

# Experimental study of turbulence, sedimentation, and coignimbrite mass partitioning in dilute pyroclastic density currents

Benjamin J. Andrews <sup>a,\*</sup>, Michael Manga <sup>b</sup>

<sup>a</sup> Department of Mineral Sciences, National Museum of Natural History, Smithsonian Institution, United States

<sup>b</sup> Department of Earth and Planetary Science, UC Berkeley, United States

## ARTICLE INFO

### Article history:

Received 22 June 2011

Accepted 17 February 2012

Available online 3 March 2012

### Keywords:

Pyroclastic density current

Experiments

Turbulence

Pyroclastic deposits

## ABSTRACT

Laboratory density currents comprising warm talc powder turbulently suspended in air simulate many aspects of dilute pyroclastic density currents (PDCs) and demonstrate links between bulk current behavior, sedimentation, and turbulent structures. The densimetric and thermal Richardson, Froude, Stokes, and settling numbers match those of natural PDCs as does the ratio of thermal to kinetic energy density. The experimental currents have lower bulk Reynolds numbers than natural PDCs, but the experiments are fully turbulent. Consequently, the experiments are dynamically similar to the dilute portions of some natural currents. In general, currents traverse the floor of the experimental tank, sedimenting particles and turbulently entraining, heating, and thermally expanding air until all particle sediments or the currents become buoyant and lift off to form coignimbrite plumes. When plumes form, currents often undergo local flow reversals. Current runout distance and liftoff position decrease with increasing densimetric Richardson number and thermal energy density. As those parameters increase, total sedimentation decreases such that > 50% of initial current mass commonly fractionates into the plumes, in agreement with some observations of recent volcanic eruptions. Sedimentation profiles are best described by an entraining sedimentation model rather than the exponential fit resulting from non-entraining box models. Time series analysis shows that sedimentation is not a constant rate process in the experiments, but rather occurs as series of sedimentation–erosion couplets that propagate across the tank floor tracking current motion and behavior. During buoyant liftoff, sedimentation beneath the rising plumes often becomes less organized. Auto-correlation analysis of time series of particle concentration is used to characterize the turbulent structures of the currents and indicates that currents quickly partition into a slow-moving upper portion and faster, more concentrated, lower portion. Air entrainment occurs within the upper region. Turbulent structures within the lower region track sedimentation–erosion waves and indicate that eddies control deposition. Importantly, both eddies and sedimentation waves track reversals in flow direction that occur following buoyant liftoff. Further, these results suggest that individual laminations within PDC deposits may record passage of single eddies, thus the duration of individual PDCs may be estimated as the product of the number of laminations and the current's turbulent timescale.

Published by Elsevier B.V.

## 1. Introduction

Pyroclastic density currents (PDCs) rapidly transport and deposit volcanic material over large areas, and the buoyant coignimbrite plumes generated by currents can inject tephra into the stratosphere, dispersing ash and aerosols over 1000 s of kilometers (Wilson, 2008). Because PDCs are 100 s of meters thick, travel at speeds generally > 30 m/s, and are composed of hot (often > 500 °C) particles turbulently suspended in air, they present substantial proximal hazards to people and structures (Bursik et al., 1998; Druitt et al., 2002; Macias et al., 2008; Dellino et al., 2010), and coignimbrite plumes formed by the lift-off of PDCs pose distal hazards to aviation (e.g. Woods and Kienle, 1994; Calder et al., 1997). Understanding the behavior of PDCs is thus critical

to interpreting ancient eruptions and predicting and mitigating future hazards. Unfortunately, direct observational records do not exist for prehistoric eruptions or are fragmentary for many historic eruptions, and the interiors of PDCs are impossible to directly observe because of their size, velocity and temperature.

Deposits provide insights into PDCs not otherwise available. Analyses of deposit grain size distributions and componentry provide a direct record of at least some portion of the particles transported by currents and changes in the composition of deposits can be used to infer spatial or temporal changes in current behavior and the ability, or lack thereof, of the current to transport particles (Cole, 1991; Branney and Kokelaar, 1997; Sparks et al., 1997; Bryan et al., 1998; Calder et al., 2000; Branney and Kokelaar, 2002; Brown and Branney, 2004; Browne and Gardner, 2005; Vasquez, and Ort, 2006; Dufek and Bergantz, 2007). Structures within the deposits, such as bedding, grading, or cross-stratification, reflect properties of the transporting current, such as its duration or steadiness (Cole, 1991; Branney and Kokelaar,

\* Corresponding author. Tel.: +1 202 633 1818; fax: +1 202 357 2476.  
E-mail address: [andrewsb@si.edu](mailto:andrewsb@si.edu) (B.J. Andrews).

1997; Sparks et al., 1997; Bryan et al., 1998; Calder et al., 2000; Branney and Kokelaar, 2002; Brown and Branney, 2004; Houghton et al., 2004; Vasquez and Ort, 2006). Two substantial problems, however, often arise when inferring current behavior from deposits. First, coupling between the transport and depositional systems within a PDC is poorly understood, thus interpretation of sedimentary structures and the relationship between deposits and currents is controversial (Branney and Kokelaar, 2002; Brown and Branney, 2004). Second, not all particles that initially contribute to PDCs are deposited within “PDC deposits.” Indeed large fractions of particles are elutriated into buoyant coignimbrite plumes whose deposits are often areally extensive but very thin and easily eroded, resulting in large uncertainties in the initial properties of currents and the volumes and extent of PDC and coignimbrite deposits (Sigurdsson and Carey, 1989; Fierstein and Nathenson, 1992; Calder et al., 1997; Branney and Kokelaar, 2002).

Scaled laboratory experiments provide a means of analyzing both the transport of PDCs as well as some aspects of the resulting deposits. In particular, time-series analysis of the currents and deposits can identify relationships between flow behavior, turbulent structures, and deposition. Coignimbrite mass can be calculated from the difference between the initial current mass and that of the deposit. Because many aspects of PDC behavior depend upon the entrainment and thermal expansion of a compressible fluid (e.g. Woods and Kienle, 1994; Bursik and Woods, 1996; Freundt, 2003; Dufek and Bergantz, 2007; Doronzo, et al., 2010), our experiments are conducted using warm particles turbulently suspended in air. We will show that the bulk, turbulent, and thermal properties of the currents and sediment are properly scaled, thus these laboratory experiments are dynamically similar to dilute natural PDCs.

## 2. Background

PDCs are mixtures of hot particles transported through a combination of turbulent, tractional, and granular processes. As these mixtures are more dense than the atmosphere, they flow as density currents. The generally accepted model of PDCs is that these currents are often stratified into two regions: a lower, denser region, and an upper, more dilute region (Branney and Kokelaar, 2002; Gardner et al., 2007). The terms *pyroclastic flow* and *pyroclastic surge* are often used for dense and dilute end-members of current behavior. It should be noted, however, that a continuum should exist in PDC density and stratification (Burgisser et al., 2005), thus in this paper we will refer to dense and dilute PDCs. Although a dense undercurrent often underlies the dilute region, dilute lobes have been observed to propagate ahead of the denser undercurrent; such lobes are then overridden by the main current (Fujii and Nakada, 1999). In general, the dense portions of PDCs are often confined to valleys and topographic lows whereas the dilute overcurrents can overtop substantial topographic barriers (Fisher et al., 1993; Gardner et al., 2007; Andrews and Manga, 2011). Although this difference in flow behavior can separate the dense and dilute portions of a PDC, flows can evolve surges and surges can generate flows, thus deposits from “dense” currents can be found on the lee side of topographic barriers that blocked the PDC undercurrent but were surmounted by the dilute overcurrent (Bursik et al., 1998; Bursik and Woods, 2000; Druitt et al., 2002; Gardner et al., 2007).

There is now general acceptance that deposits form aggradationally, rather than en masse (Dade and Huppert, 1996; Branney and Kokelaar, 1997; Calder et al., 2000; Branney and Kokelaar, 2002), even in dense flows (e.g., Lube et al., 2004; Girolami et al., 2010). Consequently, both massive “flow” deposits and stratified “surge” deposits are deposited in a grain-by-grain fashion. Numerous questions and controversies remain, however, regarding the nature and timescales of deposition and their relation to transport. Stratigraphic complexity of proximal PDC deposits suggests a complex variation in transport and depositional behavior over lateral scales of <100 m (Cole, 1991; Bryan et al., 1998; Calder et al., 2000; Houghton et al., 2004; Vasquez and Ort, 2006). Erosional

contacts between PDC depositional units record erosion of early deposits by later currents, but the extent and duration of erosion and duration of deposition remain poorly constrained (Sparks et al., 1997; Calder et al., 2000). Cross-stratified deposits are thought to reflect turbulent deposition (Branney and Kokelaar, 2002), but it is not known which turbulent structures control deposition (e.g. the largest eddies that may span the thickness of the current or smaller structures nearer the substrate).

Coignimbrite plumes are generated by PDCs when at least some portion of the current becomes less dense than the ambient atmosphere (Woods and Kienle, 1994; Bursik and Woods, 1996; Calder et al., 1997). The density of PDCs evolves during transport through sedimentation and entrainment of particles, and the turbulent entrainment and thermal expansion of air (e.g. Bursik and Woods, 1996; Dufek and Bergantz, 2007). Because dilute overcurrents have lower densities and entrain more air than dense undercurrents, dilute regions of currents are more likely to undergo buoyancy reversal and generate coignimbrite plumes.

The fraction of tephra that enters coignimbrite plumes, and is therefore not in PDC deposits, can be quite large, complicating interpretation of PDC transport processes from analysis of PDC deposits. Mass partitioning into coignimbrite plumes of >50% is estimated for eruptions ranging in size from the 1991 Redoubt eruption (Woods and Kienle, 1994), to the B3 phase of the May 18th 1980 Mount St. Helens eruption (Carey et al., 1990), to century-scale caldera-forming eruption (e.g. Ksudach KS1; Andrews et al., 2007). In very large eruptions, partitioning is expected to be as large, but the extent and preservation of the flow deposits make accurate volume estimates difficult (Sigurdsson and Carey, 1989; Fierstein and Nathenson, 1992).

## 3. Methods

Experiments were conducted in a 6.5×1.8×0.6 m acrylic tank (Fig. 1), using heated 22±6 μm talc powder to generate dilute particle laden gravity currents in air. Talc particles were chosen for the experiments as they were available in a narrow size range, have a known density and heat capacity (2400 kg m<sup>-3</sup> and 15.56 J °C<sup>-1</sup>, respectively), and do not damage the acrylic tank. Measured masses of powder,  $m_o$ , were heated up to 80 °C above ambient temperature within an oven controlled by a proportional–integral–derivative controller (PID) and PT-100 thermistor probe. Once the powder thermally equilibrated, it was evenly loaded over a specified belt length,  $L$ , of a conveyor and the temperature of the powder,  $T_o$ , was measured with a second PT-100 probe. The conveyor was then run at a known speed,  $v_b$ , to introduce the powder into the tank at a controlled rate,  $M_o$ :

$$M_o = \frac{m_o v_b}{L}. \quad 1$$

Following each experiment, the mass of the powder that remained within the chute,  $m_d$ , was measured and the mass of powder within the current,  $m_c$ , was calculated as the difference between  $m_o$  and  $m_d$ . Ranges in experimental parameters are compiled in Table 1; parameters for all experiments are listed in Supplementary material 1.

Temperatures within the tank and the chute were measured before and after each experiment with PT-100 probes mounted ~30 cm from the inlet at heights of 5, 20.5, 35.5, 80, 124.5, and 169 cm above the tank floor and within the chute. Humidity within the tank was measured before and after each run with Extech hygrometer probes mounted at heights of 20.5 and 124.5 cm.

Experiments were illuminated from below using an array of eight 250-W halogen lamps evenly spaced at 60 cm intervals 48 cm below the centerline of the tank; the light from the array was directed through a 1.5 cm wide slit to generate a light sheet illuminating a vertical plane imaged by the cameras. The lighting array was turned on immediately before each experiment, and thus heating of the tank by the lights is considered insignificant.

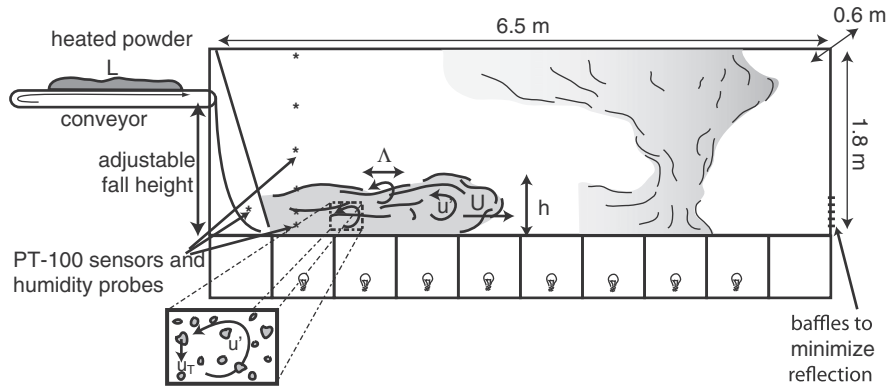


**Fig. 1.** The experimental apparatus measures  $6.5 \times 1.8 \times 0.6$  m. Experiments are illuminated with eight 250-W lamps that produce a light sheet down the tank centerline. Temperature and humidity are measured before and after each experimental run using a vertical array of PT-100 thermistor and hygrometer probes (indicated with stars). Particles are heated to the desired temperature in a PID controlled oven (not shown), then evenly loaded onto length  $L$  of a conveyor belt. The conveyor is run at a controlled speed to deliver particles at a controlled rate down a chute. Dilute density currents form at the base of the chute and flow across the tank floor. Possible reflections of currents off the downstream end of the tank are minimized with baffles that open into a passive exhaust chute. Experiments are recorded with 4 high definition (HD) video cameras.

Initial velocities,  $u_c$ , and current thicknesses,  $h$ , were measured from each experiment, and were used to calculate the temperature and density of the currents as they exited the chute. The initial mass discharge of each current is

$$M_c = \frac{m_c}{t} \quad (2)$$

where eruption duration  $t$  is the interval  $L/v_p$ . Initial particle concentration,  $C_o$ , was calculated from

$$C_o = \frac{M_c}{u_c h m_p} \quad (3)$$

where  $m_p$  is the mass per particle. Current densities and temperatures assume thermal equilibrium between particles and air within the chute such that the mixture that exits the chute with concentration  $C_o$  and thickness  $h$  has a temperature given by the equation

$$T_c = T_{c \text{ chute}} + \frac{m_c C_{p, \text{ talc}} (T_o - T_{\text{chute}})}{C_{p, \text{ curr}} (m_c + m_{\text{chute}})} \quad (4)$$

where  $C_p$  denotes the heat capacities of the talc powder ( $15.56 \text{ Jg}^{-1} \text{ } ^\circ\text{C}^{-1}$ ) and air ( $1.05\text{--}1.16 \text{ Jg}^{-1} \text{ } ^\circ\text{C}^{-1}$ , varying with temperature and humidity) within the chute, and  $m_{\text{chute}}$  is the mass of air

**Table 1**

Ranges in experimental run parameters. *Duration* is the time interval over which particles are supplied to the experiments;  $\Delta\rho$  is the difference between current and atmospheric densities;  $\Delta T$  is the difference between current and ambient temperatures;  $h$  is current thickness;  $U$  is mean current velocity;  $h$  is the current thickness;  $Re$  is the bulk Reynolds number;  $Ri$  is the densimetric Richardson number;  $TE_p/KE$  is the ratio of buoyant thermal to kinetic energy; *Runout* is runout distance; *Runout\** is the dimensionless runout;  $L$  is the ratio of liftoff position to runout distance;  $m_{\text{curr}}$  is the mass of the current;  $f_{\text{coig}}$  is the current mass fraction that enters the coignimbrite plume;  $Wall/h$  is the ratio of wall height to current thickness. The parameters of individual experiments are presented in Supplementary material.

Duration	(s)	12.7–72.7
$\Delta\rho$	( $\text{kg/m}^3$ )	0.007–0.104
$\Delta T$	( $^\circ\text{C}$ )	0–20.1
$h$	(cm)	12–21
$U$	( $\text{cm/s}$ )	8.5–19.9
$Re$		522–1476
$Ri$		0.5–18.3
$TE_p/KE$		0–8.66
<i>Runout</i>	(cm)	179–>500
<i>Runout*</i>		0.14–0.55
$L$		0.35–1
$m_{\text{curr}}$	(g)	6.2–68.4
$f_{\text{coig}}$		0–0.93
$Wall/h$		0–2.8

contained within the current, calculated as the product of air density within the chute, the height, width, velocity, and duration of the current. The current densities are calculated using the temperature from Eq. (4), air density, and specific heats as a function of temperature and humidity, and the initial particle concentration:

$$\rho_c = \frac{m_c}{tUhw} + \rho_{\text{chute}} \quad (5)$$

where  $w$  is the tank width (60.4 cm) and  $\rho_{\text{chute}}$  is the air density within the chute at the start of the experiment calculated using Eq. (4). The density of ambient air,  $\rho_{\text{atm}}$ , in the lower portion of the tank is calculated as a function of the average temperature and humidity within the lower 35 cm of the tank.

Experiments were conducted with and without topographic barriers. Barriers were built of 1.9-cm thick plywood oriented vertically (on-edge) with heights of 4.8, 7.5, and 17.8 cm, and of 0.8 cm wide Lego® bricks to heights of 8, 15, 30 and 45 cm. All walls spanned the full width of the tank. Barriers were placed at distances of 120, 180, and 240 cm from the source.

Experiments were recorded with 4 Canon HF-S100 Vixia HD camcorders with stock lenses and apertures of 2.0. The cameras were spaced at 1.3 m intervals with fields of view that overlapped  $\sim 5$  cm in the light sheet. Experiments were recorded at 30 fps (deinterlaced) and  $1920 \times 1080$  pixel resolution, corresponding to a nominal pixel size of  $\sim 0.7$  mm/pixel. Because the cameras internally compress the image files, the functional resolution, e.g. the smallest features within the currents that are easily resolved, is  $\sim 7$  mm in processed images. Although the functional resolution of these consumer grade cameras is far too coarse for identifying and tracking individual particles, it is more than adequate for identifying and tracking large-scale structures within the currents. Similarly, the camera frame rate is well-suited for tracking turbulent structures in our modeled currents; it should be noted that higher frame rates (e.g. 1000 fps) would result in impractically large data sets that would require decimation prior to processing. Data processing begins with conversion of the video files into grayscale image series. Barrel distortions were removed from each image series using Adobe Photoshop®, and all subsequent processing was performed using MATLAB®. Lighting corrections based upon distance from each lamp were made and grayscale intensities less than the average background intensity measured prior to each experiment were set to 0 to facilitate flow visualization and image processing; that threshold value corresponds to the grayscale intensity of the rear wall of the tank prior to each experimental run. Processed images are stitched together to form single time series for each experiment. The stitched grayscale images are converted into concentration fields by dividing the initial

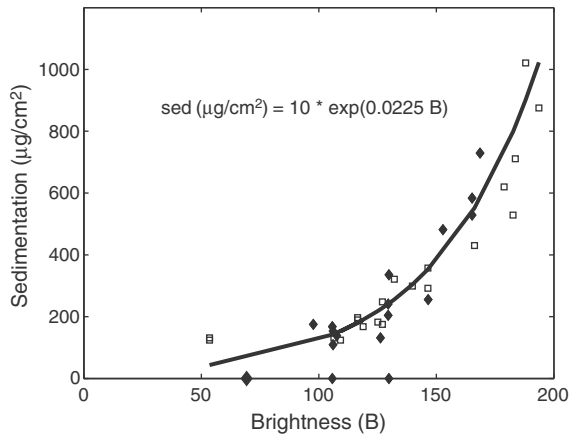


**Fig. 2.** Measured sedimentation as a function of brightness ( $B$ ) along the tank floor for experiments 080310-1 (open squares) and 080310-2 (filled diamonds). An exponential fit to 080310-2 ( $R^2=0.83$ ) also shows good agreement with 080310-1 ( $R^2=0.85$ ) and shows that sedimentation calculated from brightness is reproducible.

particle concentration by the average gray-scale intensity of the current 10 cm downstream from the outlet. We assume that for the very dilute currents we generated, the relationship between concentration and brightness is linear over the concentration range within the experiments (particle concentrations  $<0.003$  vol.%). This assumption implies a concentration of  $\sim 0.013$  vol.% above which the camera detectors would saturate. Importantly, however, many of the analyses presented below do not rely on the absolute particle concentration, but instead depend on relative changes in concentration or brightness, and brighter regions correspond to higher particle concentrations.

We characterize turbulence with the autocorrelations,  $R_c(t)$ , through time of the concentration at each position

$$R_c(t) = \frac{1}{n} \sum_{i=t_n}^{t_f-t} \frac{(C_i - C_{avg})(C_{i+t} - C_{avg})}{C_{var}} \quad 6$$

where  $n$  is the number of correlation pairs with lag time  $t$  in the time series ( $t_0$  to  $t_f$ ) of interest,  $C_i$  and  $C_{i+t}$  are the concentration at times  $i$  and  $i+t$ , and  $C_{avg}$  and  $C_{var}$  are the average and variance in concentration over the time series. The characteristic, zero-correlation timescale is measured as the lag time,  $t$ , at which  $R_c$  first reaches zero (Andrews et al., 2011). These timescales, hereafter referred to as “turbulent timescales”, are similar to integral timescales of turbulent fluctuations in concentration, and represent the time it takes for the largest turbulent structures to pass a particular position (Bernard and Wallace,

2002). Because the currents are transient and evolve with space and time, the timescales are calculated over total lag times of 6 s at intervals of 1 s. To facilitate data processing, timescales are calculated on a uniform 4-pixel grid. Although these timescales are calculated for a two-dimensional plane, whereas the flow is three-dimensional, the timescales describe streamwise variation in the turbulent field and should be representative of three-dimensional structures within the currents assuming that the turbulent field is not highly anisotropic.

Deposit mass per unit area, termed “sedimentation,” was measured for two experiments at 18 and 20 positions along the floor of the tank. The measured masses ranged from  $7 \times 10^{-4}$  to  $8.4 \times 10^{-3}$  g corresponding to  $\sim 10^{-4}$  to  $10^{-3}$  g  $\text{cm}^2$ . The light intensity along the centerline of the tank floor was measured from the corrected images at the end of the experiment when all particles had settled. Measured sedimentation,  $S$ , is proportional to measured brightness,  $B$ , (Fig. 2), permitting calculation of sedimentation in units of  $\text{mg cm}^{-2}$  with the expression

$$S(B) = 10 \times \exp(0.0225 B) \quad 7$$

The tank floor is always the brightest part of the field of view (greater than a factor of 2) and we consider any illumination of the floor by light scattered from turbulently suspended particles to be minor. As a result sedimentation can be calculated as a function of time and space for all experiments using the time series of brightness at the tank floor. Sedimentation rate as a function of position,  $x$ , and time,  $t$ , is calculated as

$$S_{rate} = \frac{S_{t+1.5s} - S_{t-1.5s}}{3s} \quad 8$$

Sedimentation rate is calculated over time intervals of 3 s, corresponding to the longest turbulent timescales generally observed in the currents.

The coignimbrite mass,  $m_{coig}$ , is calculated as the difference between  $m_{curr}$  and  $m_{sed}$ , the integrated deposit mass over the tank floor. The ratio  $m_{coig}/m_{curr}$  describes mass partitioning into the coignimbrite plume.

The relevant bulk and turbulent scaling parameters are defined in Table 2. Although the Reynolds numbers of our experiments are substantially lower than those of natural, dilute PDCs, the modeled currents are fully turbulent and the other dimensionless numbers are within the range of natural PDCs. Thus we are confident that the experiments capture the large scale dynamics of some dilute PDCs.

We estimate measurement uncertainties of  $<3\%$  for  $U$ ,  $10\%$  for  $h$ ,  $<3\%$  for  $m_c$ ,  $10\%$   $m_{sed}$ , and  $<0.2$  °C for temperatures. Those measurement uncertainties correspond to uncertainties of  $17\%$  for  $C_o$ ,  $17\%$  for  $\rho_c/\rho$ ,  $10\%$  for  $m_{coig}$ ,  $13\%$   $m_{coig}/m_{curr}$ , and  $4\%$  for  $\Delta T$ . Energy densities

**Table 2**

Scaling and expressions for energy densities of experimental currents and natural PDCs. The bulk current and atmospheric densities are denoted with  $\rho_c$  and  $\rho_{atm}$ , respectively,  $\Delta\rho$  is their difference, and  $\rho_p$  is particle density. The mean, turbulent, and particle fall velocities are given as  $U$ ,  $u'$  and  $u_f$ . Gravity and reduced gravity are shown as  $g$  and  $g'$ . Current thickness is given as  $h$ , and the characteristic turbulent length scale as  $\Lambda$ . The coefficient of thermal expansion for air is given as  $\alpha$ .  $C_{p,curr}$  and  $C_{p,atm}$  are the bulk heat capacities of the current and atmosphere, and the temperature difference between the current and atmosphere is indicated with  $\Delta T$ . The characteristic particle response time,  $\tau_v$  is calculated using the methods described by Burgisser et al. (2005).  $f$  is a particle drag coefficient. Values for natural dilute PDCs are from Burgisser et al. (2005), except for the estimate of  $Fr$  that is based on scaling arguments for gravity currents (e.g. Simpson, 1997). Table was modified from Table 1 in Andrews and Manga (2011).

		Natural dilute PDCs	Experiments	Description
Re	$\frac{\rho_c U h}{\mu}$	$10^6 - 10^9$	$10^3$	Ratio of turbulent to viscous forces
Ri	$\frac{g' h}{\rho_{atm} U^2}$	0–10	0–20	Stratification stability. $Ri > 10$ indicates unstable stratification; $Ri < 1$ indicates stable stratification; $1 < Ri < 10$ indicates transitional behavior.
$Ri_T$	$\frac{g' \alpha h}{U^2}$	0–5	0–5	Ratio of buoyant to forced convection, $Ri_T < 0.1$ indicates negligible buoyant convection; $Ri_T > 10$ indicates negligible forced convection; $1 < Ri_T < 10$ suggests a combination of behaviors
Fr	$\frac{U}{\sqrt{g' h}}$	$\sim 1$	$\sim 1$	Inertial to gravitational forces.
$S_T$	$\frac{\rho_c u_f \Lambda}{f \Lambda} \left(1 + \frac{\rho_c}{2\rho_p}\right)$	0.01–200	$10^{-4}$	Coupling of particles to turbulent motion. $S_T < 1$ indicates complete coupling; $S_T > 1$ indicates complete decoupling; $S_T - 1$ indicates particle cluster along eddy margins.
$\Sigma_T$	$\frac{u_f}{u'}$	$10^{-6} - 10^5$	$< 1$	Ratio of particle settling velocity to turbulent component of fluid velocity. $\Sigma_T < 1$ indicates suspension; $\Sigma_T > 1$ indicates sedimentation.
KE	$\frac{\rho_c U^2}{2}$	$10^3 - 10^4$ J/m <sup>3</sup>	0.01–0.04 J/m <sup>3</sup>	Kinetic energy density.
$TE_b$	$\frac{\rho_c C_{p,curr}}{\rho_c C_{p,atm}} \alpha T g h$	$10^3 - 10^4$ J/m <sup>3</sup>	0–0.2 J/m <sup>3</sup>	Buoyant thermal energy density.

have uncertainties of 15% for  $TE_b$ , and 17% for  $KE$ ; the ratio  $TE_b/KE$  has an uncertainty of 14%.

#### 4. Results

A list of experiments is presented in Supplemental material 1 and movies of an experimental current, its sedimentation rate, and its turbulent timescales are presented in Supplementary material 2. Laboratory density currents generated in our experiments have initial thicknesses  $h_o$  of 0.15–0.25 m, initial current head velocities of 0.1–0.2 m/s, temperatures 0–10 °C greater than ambient, and initial densities of ~1.21–1.25 kg/m<sup>3</sup>, corresponding to particle concentrations of ~0.0007–0.003 vol.%. Atmospheric density within the tank ranges from 1.18 to 1.23 kg/m<sup>3</sup> during experiments. Current heads generally have lengths that are 3–4 times the current thickness and form the thickest portions of the currents (Fig. 3). The current heads are followed by tails with thicknesses typically two-thirds as those of the heads. Variation in the duration of experiments does not noticeably affect the length of current heads, but does affect the current tails such that short-duration experiments generate currents that are composed almost entirely of the head, whereas longer-duration currents have well-developed tails. Current thicknesses increase during transport prior to current liftoff, with thicknesses approximately doubling over 3 m of transport; current thickness is roughly proportional to the square root of the distance traveled.

Current runout distances range from 1.8 to 4.8 m. For comparison between experiments and with natural currents, we have normalized the measured runout distance with that predicted by the ratio of current speed and thickness to the Stokes settling velocity of the particles.

$$Runout^* = \frac{Runout}{hU/u_T} \quad 9$$

The normalized runout distance decreases with increasing  $TE_b/KE$ , such that hot currents with  $TE_b/KE > 4$  propagate only 20% as far as currents that begin in thermal equilibrium with the atmosphere (Fig. 4). Buoyant liftoff generally occurs near the maximum runout position or, if currents traverse barriers, above topographic obstructions; the effects of topography on PDC behavior are discussed more fully in Andrews and Manga (2011).

During horizontal propagation (as opposed to buoyant liftoff), the largest turbulent structures form along the top of the current. In general, the forward-most appearance of those eddies is at the rear of the current head, although occasional large structures grow from instabilities that develop along the nose and leading edge of the head. In well-developed tails, growth of Kelvin–Helmholtz instabilities at the interface of the currents and atmosphere generates large, regularly-spaced eddies (Fig. 5). The largest eddies typically have streamwise length scales of  $h$  and heights of 0.25–0.5  $h$ . Smaller eddies are readily apparent as components of the larger structures and as independent features.

As currents approach their termini, their velocities decrease and thicknesses increase (Fig. 3). Notably, the combination of those two changes often results in the formation of a sharp, vertical, nearly stationary, and sustained “wall” at the end of the current (Fig. 3): particles remain in turbulent suspension on one side of the interface,

whereas the other side comprises uncontaminated air. When liftoff begins, this boundary recedes slightly at the base of the current. As liftoff progresses, eddies form on the margins of the rising plumes; the turbulent structures on the upstream and downstream sides of the plumes have length scales of  $\sim h$ . The current tails generally appear to transition directly into the rising plumes, with occasional pulses of material remaining non-buoyant and on the tank floor. A recirculating structure often forms at the forward edge of the currents beneath the rising plume; this structure does not lift off, but remains at the base of the plume and is periodically resupplied by denser pulses from the tail. When the conveyor ceases to feed particles into the tank and the current tails no longer supply mass and thermal energy to the buoyant plume, the plume detaches from the base of the tank. Detachment generally begins at the distal end of the current and “rolls back” toward the source, resulting in a series of eddies that propagates upstream beneath the rising and detaching plume (Fig. 3). Importantly, those eddies propagate upstream with speeds comparable to the earlier, downstream current transport ( $> 0.1$  m/s).

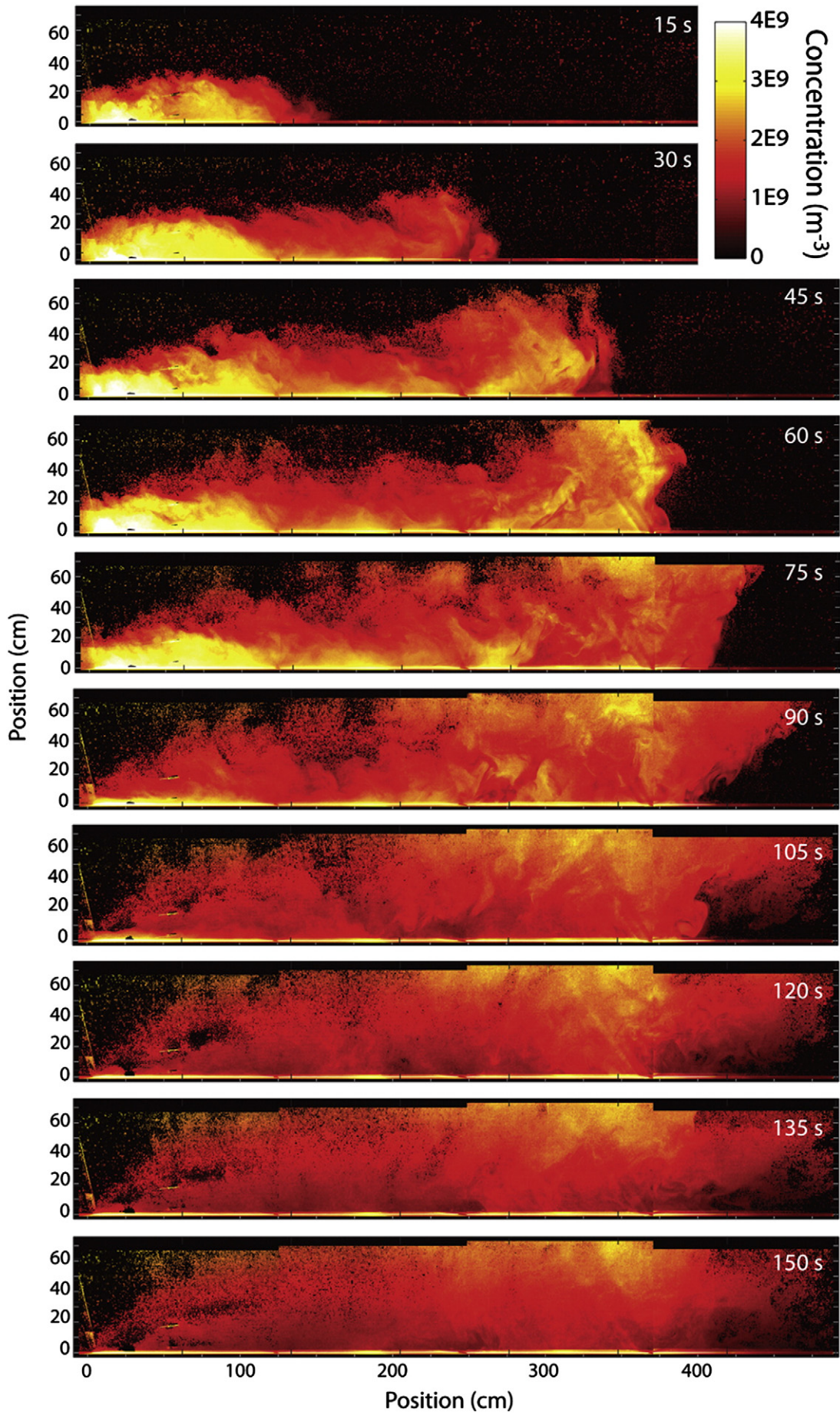
##### 4.1. Sedimentation

Deposit mass per unit area (sedimentation) varies systematically within each experiment as a function of distance and time. In general,  $m_{sed}$  can range from 0.1 to 1.0 of  $m_{curr}$ ; the fraction sedimented varies with  $Ri$ , thermal energy, and topography (Fig. 6). Deposit mass decreases with distance from the source for every current. The form of the decrease, however, is not uniform between different currents: cold currents tend to show very steep initial decreases followed by a gradual decline in sedimentation over the remaining 90% of the traveled distance, whereas the initial decrease in hotter currents occurs over a greater distance relative to the total runout. Sediment deposition does not show exponential decay with distance. In some currents, deposition increases slightly in the vicinity of the liftoff position.

Sedimentation decreases with increasing  $Ri$  number and thermal energy density (Fig. 7). In general, the mass fraction sedimented decreases approximately by a factor of 2 as  $Ri$  increases from 0 to 2, 2 to 4, and 4 to 8. The effects of thermal energy density follow a similar pattern, with sedimentation halving as  $TE_b/KE$  increases from 0 to 2 and from 2 to 4. As either  $Ri$  or  $TE_b/KE$  increase, sedimentation decays at a reduced rate with distance such that stably stratified or cold currents have steeper initial decreases in sedimentation. Net sedimentation at each position is proportional to the time averaged particle concentration above that position (Fig. 7).

Topographic barriers affect both the total deposit mass fraction and the deposit profile, most likely because walls can focus buoyant liftoff and arrest runout (Andrews and Manga, 2011). In general, as wall height increases, the mass fraction sedimented decreases; this effect is most pronounced in currents that encounter obstructions comparatively early. Because tall barriers can terminate forward flow propagation, deposits of currents that encounter large obstructions extend over a shorter distance and are thicker at their termini than those from similar currents that traverse a flat terrain. Currents that transit barriers often run out as far as similar currents that transit flat topography, but the resulting deposits downstream of the walls are thinner.

**Fig. 3.** Images of current 062510-3 as it propagates across the tank and lifts off. Particle concentration is indicated by color. Initially, the current is <30 cm thick, and shows a well developed head with apparently minor mixing. By 30 s, however, Kelvin–Helmholtz instabilities have formed along the upper surface of the current following the head, and the thickness of the head has increased. The current has also begun to segregate into a more concentrated lower region and more dilute upper region. From 45–60 s, the degree of mixing along the top of the current increases, and the thicknesses of the current head and tail grow; this is particularly apparent in the head, where the current begins to lift off as its forward motion slows. By 75 s the current has essentially reached its maximum runout distance and an increasing fraction of particles are directed upward into the rising plume; at this time introduction of particles into the tank ceases. More proximal portions of the current begin to lift off such that by 90 s the base of the plume occupies approximately half of the total runout distance, and the plume begins to noticeably spread downstream at heights  $> 40$  cm. Nearly all portions of the current have essentially stopped forward motion by 105 s, but the plume remains attached to the tank floor as an upstream propagating eddy begins to form at the downstream base of the plume. That eddy is still apparent as a high concentration region near the floor at positions of ~350 cm and 300 cm at 120 and 135 s, respectively. By 150 s, the plume is essentially detached from the tank floor.



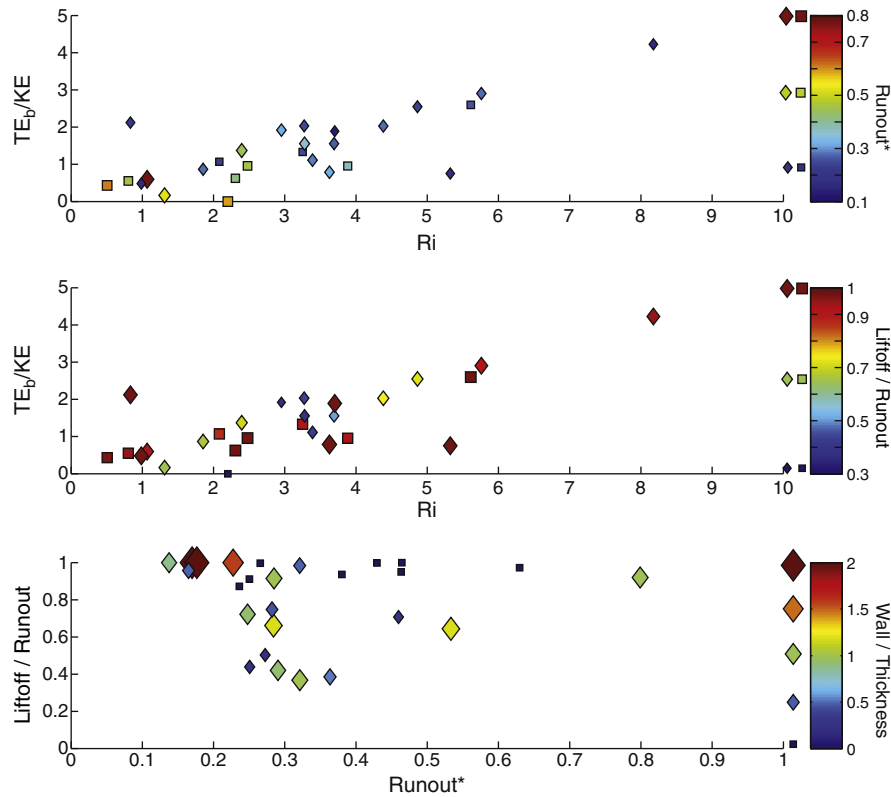


**Fig. 4.** a) Runout\* decreases with both Ri and  $TE_b/KE$ , showing that as stratification stability decreases or excess thermal energy increases, the rates of air entrainment and expansion increase, resulting in faster decreases in current density, and thus reduced runout distance. Runout\* is indicated by both symbol size and color. b) Liftoff is focused near the distal ends of most currents ( $Liftoff/Runout = >0.85$ ), and is largely unaffected by Ri or  $TE_b/KE$ ; exceptions to this pattern are currents with comparatively earlier liftoff focused near topographic barriers that the currents overtopped. Liftoff position is indicated by symbol size and color. c) Liftoff position is highly dependent on the height of topographic barriers, such that obstructions with thickness  $>1.5h$  are not surmounted (Andrews and Manga, 2011). In general, currents with Wall/Thickness = 0 lift off near the current termini, currents with Wall/Thickness  $>1.5$  do not pass the obstructions and thus lift off at the barriers, but currents that encounter barriers with height  $<1.5h$  undergo enhanced air entrainment and buoyancy generation near the obstructions. Wall/Thickness is indicated by symbol color and size.

#### 4.2. Coignimbrite mass partitioning

Mass fractionation into the coignimbrite plume ranges from 0 to 0.9. In general, fractionation into the coignimbrite plumes increases with both Ri and  $TE_b/KE$  (Fig. 7). Interaction with topographic barriers may slightly increase coignimbrite fractionation, particularly in currents that encounter large barriers comparatively early (Fig. 7). The total mass that enters the coignimbrite plumes is proportional to the excess thermal energy of the currents (Fig. 7). This relationship is approximately linear:  $<5$  g enters the plume when excess thermal energy is  $<50$  J, 20–25 g separates for energies of 200–250 J, and  $>25$  g enters the plume when thermal energy exceeds 350 J.

#### 4.3. Sedimentation and erosion rates

Sedimentation and erosion rates are shown for two currents in Fig. 9 and Supplemental material 3. Sedimentation does not proceed at a constant rate during experiments, but instead particles accumulate through the apparent propagation of a series of depositional and erosional waves, pairs of which are hereafter referred to as sedimentation waves. Integrating those rates through time produces the final current deposits. The currents are net-depositional, thus although the instantaneous depositional and erosional rates are of similar magnitude (ranging from 0 to  $\sim 400 \mu\text{g cm}^{-2} \text{s}^{-2}$ , but typically  $\sim 50 \mu\text{g cm}^{-2} \text{s}^{-2}$ ), the cumulative or average rates of deposition are much lower, on the order of  $5 \mu\text{g cm}^{-2} \text{s}^{-2}$ . Both the instantaneous and average sedimentation rates decay with distance from the source.

The sedimentation waves track the current front, with the size of the first wave being the longest and similar in size to the current head, and subsequent waves are smaller. When the currents begin

to lift off, the leading sedimentation wave slows down, resulting in a merging of that first wave with several of the trailing waves (Fig. 8). When the current stops forward propagation, sedimentation often becomes disorganized behind the leading wave as persistent depositional structures are not necessarily present. During this time, sedimentation waves that were well-defined in more proximal regions deposit very little sediment beneath the rising plume.

Sedimentation waves also track roll back of buoyant plumes as they detach from the tank floor. Specifically, when detachment begins, a sedimentation wave begins from the most distal reach of the current and propagates back toward the source; such waves are often followed by a series of smaller waves that originate at the distal end of the current. The regions of disorganized sedimentation also propagate upstream, and they disrupt and engulf downstream propagating sedimentation waves.

Times series of sedimentation from currents that encounter barriers show distinct differences compared with currents that traverse flat topography (Fig. 8). First, although the first few sedimentation waves propagate toward and encounter the obstruction with little change, subsequent waves are often disrupted within 1–2 wall heights by upstream propagating waves with similar amplitudes as the downstream propagating waves. Second, the sedimentation patterns of currents that run out past the barriers show a bifurcation in sedimentation wave direction downstream from the wall where the currents reattach to the surface: minor sedimentation waves propagate upstream from the reattachment position toward the wall whereas the bulk of the current propagates downstream toward the eventual runout position. Further, short period sedimentation waves that are present upstream of the topographic barrier merge into

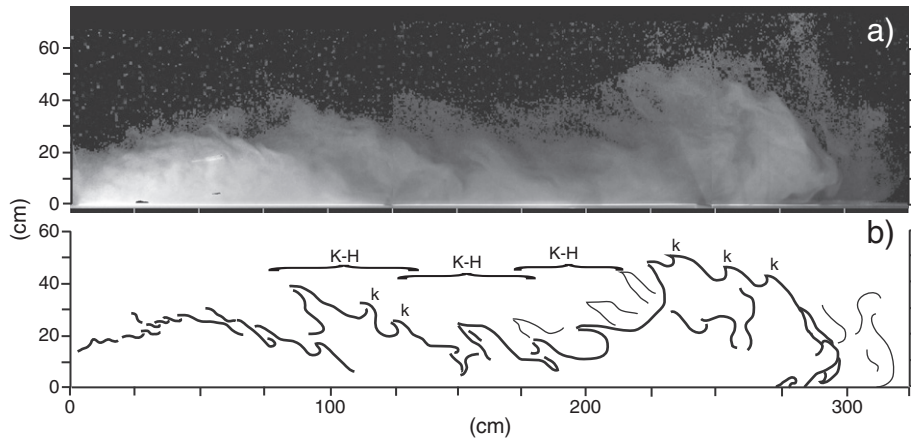


**Fig. 5.** Photograph (a) and sketch (b) of current 062510-3 at 86.33 s illustrating that turbulent structures entrain air over a range of scales. Large Kelvin–Helmholtz instabilities on the top of the current tail are indicated with bracket symbols and “K–H”; smaller instabilities on the top of those large rolls and the head are indicated with “k”.

longer period structures downstream of the reattachment point. Lastly, upstream-propagating waves resulting from flow reversals do not proceed upstream past the topographic obstruction.

4.4. Turbulent timescales

Turbulent zero-correlation timescales as functions of position are shown for several times in Fig. 10; video of these timescales are presented in the Supplementary material. Turbulent timescales of variation in particle concentration provide a means of examining mixing and entrainment within the currents and studying how those processes vary with time, position, and current behavior. Because the average current velocity is equal to the ratio of the characteristic length scale and timescale,  $U = \lambda/\tau$ , timescales can be transformed to turbulent length scales; essentially, long-period turbulent structures are equivalent to long-wavelength structures (Bernard and Wallace, 2002).

During horizontal transport, the dominant features of the currents are large, long-period (2–3 s) structures that form most of the current

head and somewhat smaller structures with similar periods that follow (Fig. 9). The structure at the current head generally spans the entire thickness of the current. Between those features are structures with much shorter turbulent periods (<1 s) that evolve quickly through time and space. Initially the trailing structures are also as thick as the currents, but as Kelvin–Helmholtz instabilities develop, the structures partition into two layers: an upper portion that moves comparatively slowly downstream and a lower region wherein eddies propagate downstream with the velocity of the current head. These two regions typically form within the initial 120 cm of transport (similar in scale to 4–5  $h_0$ ). Usually, the lower, faster moving region has a thickness of 0.3–0.5  $h_0$  throughout most of the propagation distance, whereas the thicknesses of the upper, slower regions tend to grow during transport.

When the currents reach their runout distance and begin to lift off, the turbulent field significantly changes. The large structure at the current head stretches vertically before breaking into smaller structures with similar periods (~3 s) (Fig. 9). Simultaneously, the trailing structures flow up and over the leading structure and into the

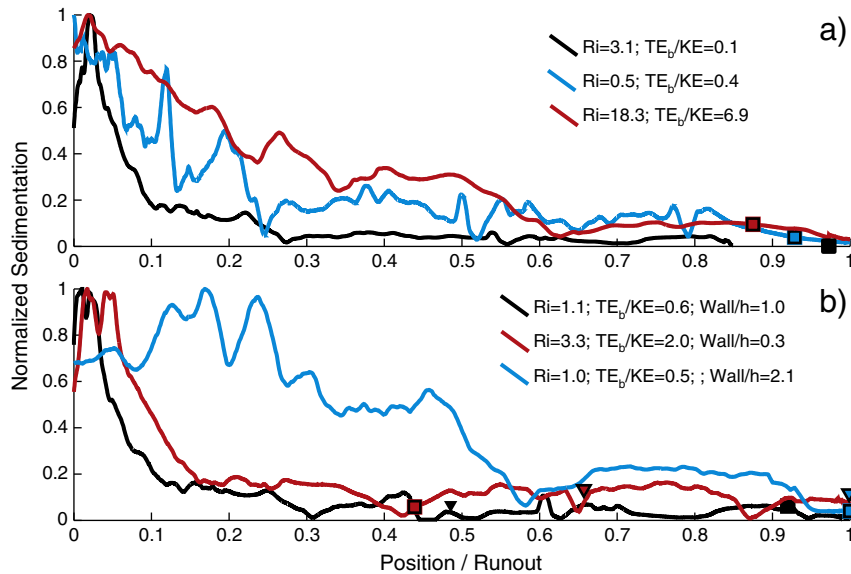


**Fig. 6.** Plots of sedimentation, normalized by the maximum deposit mass per area for each experiment, as a function of position within the deposit and Ri for currents that traverse flat topography (a) and traverse barriers (b). a) At low Ri the thickest deposits form primarily near the source, but as Ri increases, deposition is distributed over a larger fraction of current runout. Similarly, as  $TE_v/KE$  increases, the deposits spread out. b) Currents that traverse barriers show sedimentation patterns generally similar to currents in a flat terrain. The most distal deposits of currents that encounter but do not pass barriers are much thicker than for similar currents that traverse the walls. The locations of plume liftoff are indicated by squares; wall positions are shown with triangles in (b).

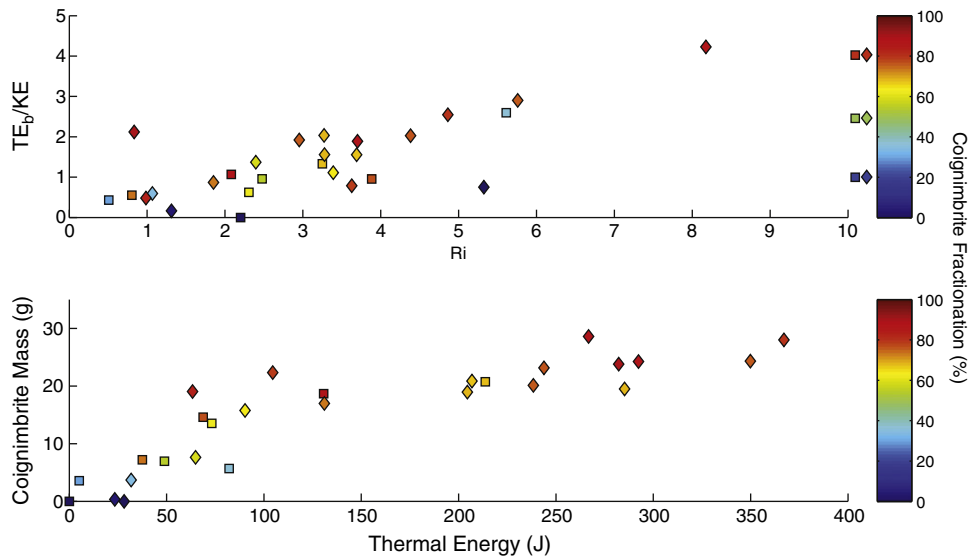


**Fig. 7.** a) Coignimbrite fractionation increases with both  $Ri$  and  $TE_b/KE$ . b) Coignimbrite mass is proportional to excess thermal energy of the currents. Coignimbrite fractionation is indicated in both plots by symbol color and size.

developing plume. As flow continues, the point at which structures detach from the base and flow upward progresses upstream and the region of small turbulent structures grows; this region develops as a complex group of convective cells with upward motion along the upstream and downstream edges, and intermittent upwelling and downwelling in the interior. The chaotic motion at the base of the plume interior appears to result from the lower, more vigorous portion of the current shedding non-buoyant eddies into the plume base; some of those non-buoyant eddies also resupply a structure that persists at the forward base of many plumes. When the last large structure propagates into the upstream side of the plume, smaller structures at the base of the convective cell at the downstream edge of the plume merge together and begin to propagate upstream as a large eddy with timescale of  $\sim 3$  s. Several smaller eddies with timescales of 1–2 s follow in the wake of that larger structure. All of these structures, large and small, lift off beneath the upstream edge of the plume.

Currents that lift off at topographic barriers often develop persistent structures at the upstream base of the barriers. Those structures are essentially bypassed by the current as it flows over the wall and lifts off, but occasionally they spread in the upstream direction for a distance equivalent to 1–2 wall heights. When currents overtop barriers they display more complexity in their turbulent structures. As a current head proceeds over an obstruction, it is initially mantled by a long timescale structure, but as the current head begins to collapse back to the tank floor, the underside of that structure breaks into a large structure that continues downstream and a small structure that propagates back toward the lee side of the barrier; this smaller structure often persists for the duration of the flow as a region of circulation underlying the main current as it flows over the wall. Downstream of the reattachment point and during buoyant liftoff, the currents behave similar to those that traverse flat topography, with the exception that rollback of eddies proceeds from the runout position upstream to the topographic barrier.

## 5. Discussion

### 5.1. Current behavior and sedimentation

Total sedimentation and coignimbrite fractionation are closely linked to current behavior and bulk current properties. First, the deposit length records the farthest extent of particle transport by ground hugging currents, notably, however, those deposits can be

quite thin in distal regions as seen both in our experiments and in natural PDCs (e.g. Wilson and Walker, 1982; Druitt et al., 2002; Vasquez and Ort, 2006). Second, the deposit profiles occasionally show secondary thickening near the location of plume liftoff suggesting the importance of sedimentation as a source of buoyancy and indicating that locally enhanced sedimentation may occur beneath some rising plumes.

Total sedimentation is highly dependent on  $Ri$  and  $TE_b/KE$ , largely because these two parameters control coignimbrite fractionation. Given that a current has some excess thermal energy, then some portion of the current will undergo a buoyancy reversal if ambient fluid is entrained and thermally expanded prior to the current sedimenting all particles (Woods and Kienle, 1994; Bursik and Woods, 1996; Calder et al., 1997). Currents with high  $Ri$  are able to more effectively entrain ambient fluid, and a higher  $TE_b/KE$  allows for more thermal expansion of each parcel of entrained fluid. Thus as  $Ri$  and  $TE_b/KE$  increase, the mass fraction sedimented decreases.

It should be noted that although our experiments were conducted using a very narrow grain size distribution, whereas those of natural dilute PDCs are much broader, the basic processes through which mass is transported and sedimented or fractionated into coignimbrite plumes should be similar in both systems. The effects of broader and coarser natural grain size distributions on the behavior of dilute PDCs are largely predictable. First, as the currents are dilute, particle–particle interactions are not significant within the transport system, and thus sedimentation of each clast size and density should occur independently. In currents with broad particle size and density distributions, we should expect that the different classes of particles have different degrees of coupling to the turbulent motions of the fluid, governed by  $S_T$  and  $\Sigma_T$  (Burgisser et al., 2005), resulting in segregation of the larger, denser particles into the lower regions of the current or the depositional system (such systems are not present in our modeled currents). If the segregation occurs relatively quickly, then the thermal energy of those particles is unavailable for thermal expansion of entrained air. More specifically, if the residence time of the particle within the dilute portion of the current is shorter than the timescale of thermal equilibration with the atmosphere,  $\sim 10^2$  s for cm-size clasts (Stroberg et al., 2010), then some of the particle's thermal energy is removed from the current. Currents enriched in coarse or dense particles will most likely have increased deposition in proximal regions, shorter runout distances, and reduced coignimbrite fractionation compared with finer-grained currents. Differential responses of the particles should also affect the

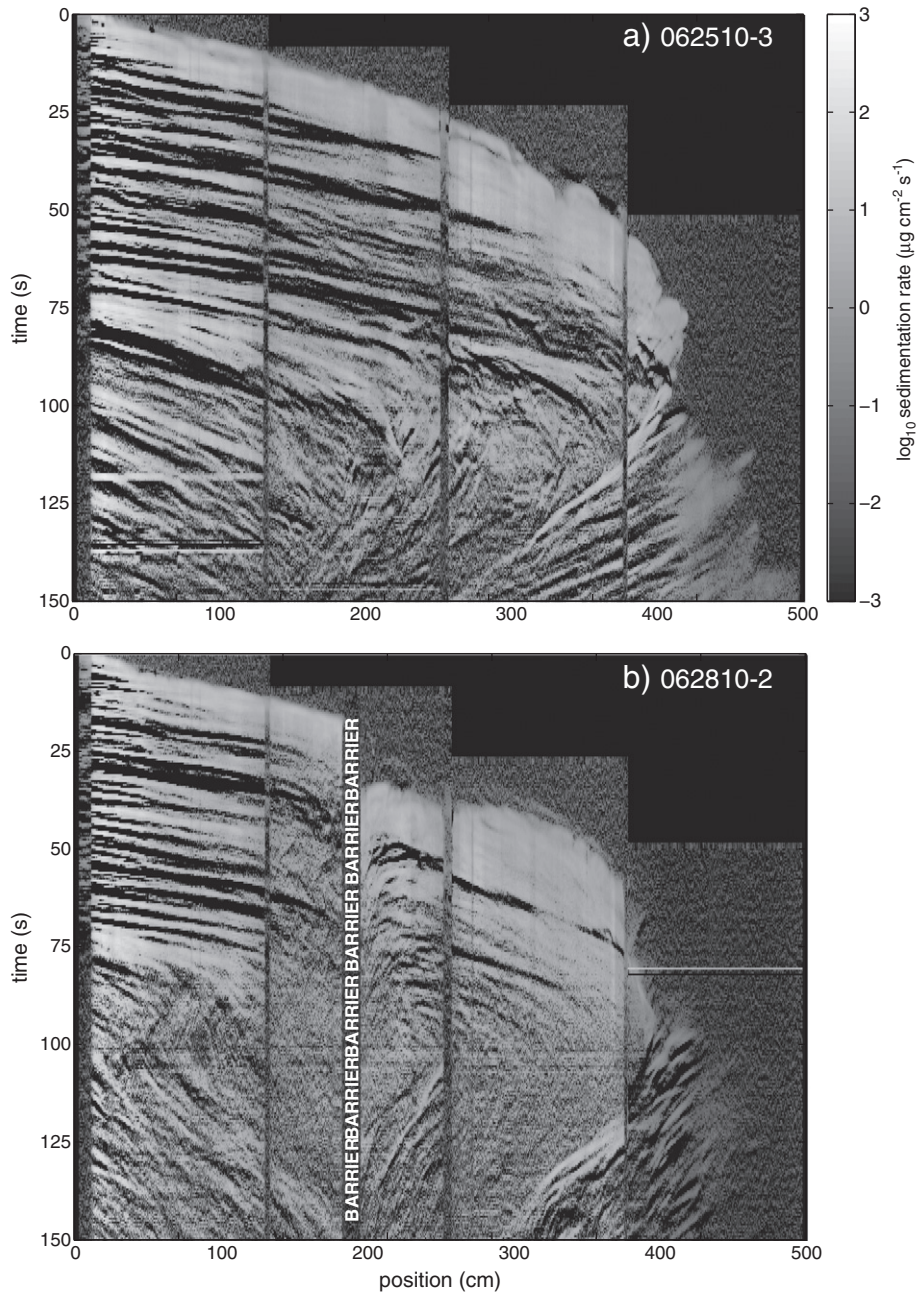


**Fig. 8.** Sedimentation rates as a function of time and distance. a) As current 062510-3 traverses a flat-bottomed tank, sedimentation occurs as a series of waves propagating with and behind the current head. Erosion intervals (black) separate each depositional interval. As the current slows and approaches its terminus, the trailing sedimentation waves merge with the lead structure. At ~90 s, depositional waves beneath the rising plume (225–375 cm) begin to break apart and an upstream propagating sedimentation wave starts to form. As that wave propagates upstream, the region of disorganized sedimentation also moves upstream. b) The sedimentation patterns of current 062810-2 are strongly influenced by a barrier located at ~180 cm. As the current head traverses the barrier, there is a delay in sedimentation before the collapsing current head reattaches the floor at ~30 s and 200–300 s. Once reattachment occurs, sedimentation waves immediately downstream of the wall propagate upstream, tracking eddies in the lee of the barrier. Upstream of the barrier, sedimentation between 150 cm and the barrier is disrupted and largely structureless. Upstream propagating sedimentation waves originate from the downstream edge of the plume beginning at ~95 s, and shorter wavelength structures propagate from ~250 cm upstream toward the barrier but do not pass the obstruction. Sedimentation rate is indicated by gray scale; erosional intervals are shown in black. Color figures of deposition and erosion are presented in Supplemental material.

degree of sorting within deposits; this is discussed in more detail in Section 5.4.

### 5.2. Coignimbrite fractionation

The total mass fractionated into coignimbrite plumes is directly proportional to the excess thermal energy of the currents, and in many currents the mass fraction that enters the plumes, which is proportional to  $Ri$  and  $TE_b/KE$ , exceeds 50%. Together, those observations suggest that the currents are very efficient at converting thermal

energy into buoyancy, which is not surprising given the small particle size, and good coupling between particle and fluid motions as indicated by  $S_T$  and  $\Sigma_T$ . Application of these relationships to natural currents indicates that understanding the timescales of air entrainment, thermal expansion, and particle residence in the transport system, specifically whether particles can transfer their heat to the entrained atmosphere prior to sedimentation, is critical to understanding the development of coignimbrite plumes.

Knowledge of the mass and thermal discharges of coignimbrite plumes is required for predicting the altitudes to which the plumes

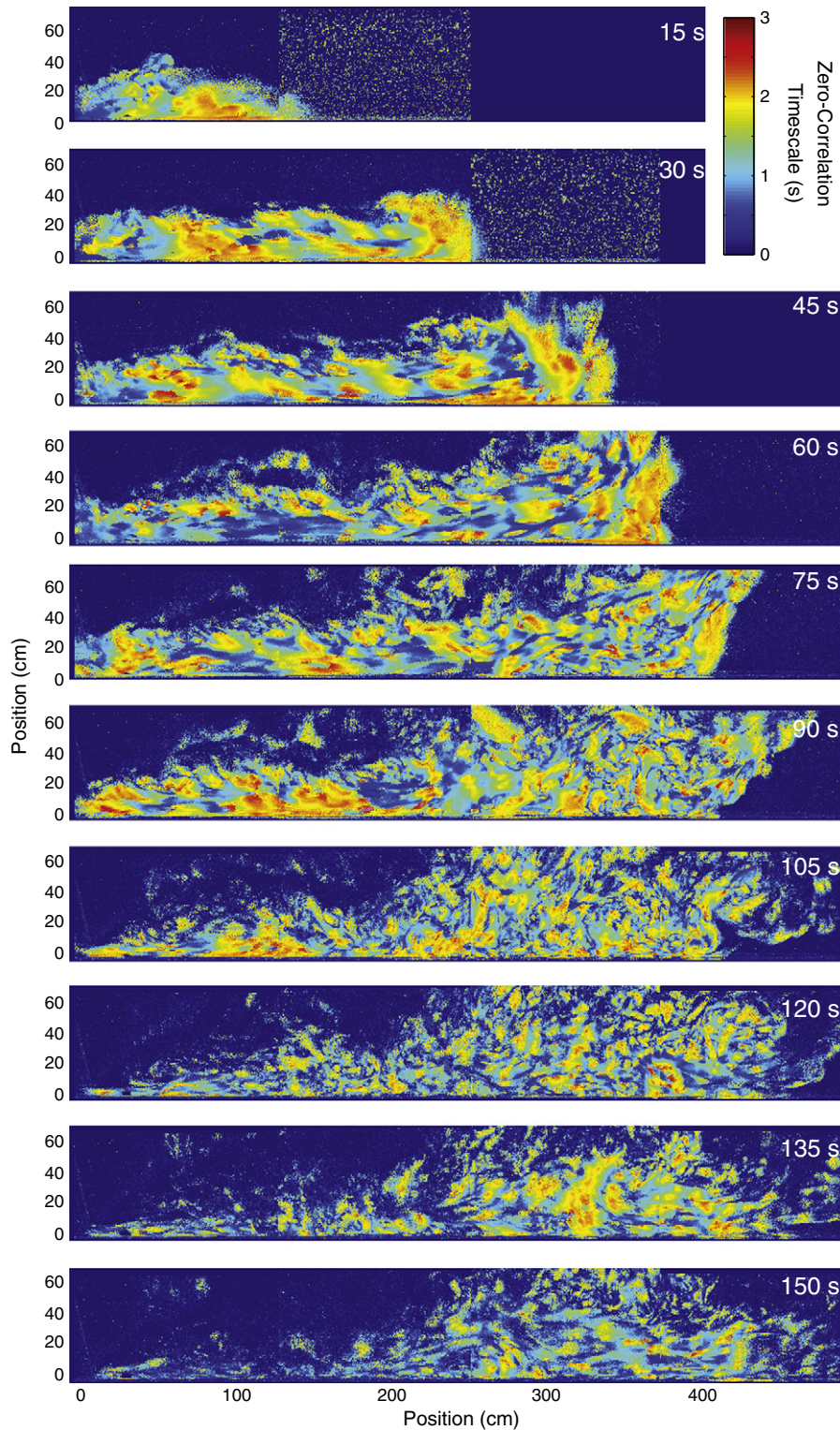


**Fig. 9.** Zero-correlation timescales of current 062510-3. The current head is generally dominated by a long-duration structure ( $\tau > 2$  s) and trailed by a series of similar timescale structures through the initial 45–60 s. Kelvin–Helmholtz instabilities are apparent as somewhat regularly spaced long-period structures along the upper surface of the current from 30 to 45 s. Concentration stratification and the development of a denser lower region are apparent from approximately 30 s onward; this stratification is generally apparent as a discontinuity in turbulent structures occurs approximately halfway up through the current. As liftoff begins (~60 s) a large, long-period structure is present at the forward base of the plume; behind this structure, the lower portion of the current appears to feed directly into the plume. By 75 s, although the large structure at the plume base remains, the trailing structures have become smaller and less organized; the transition in behavior from stratified, dominantly lateral transport to less organized structures at the plume base occurs at ~250 cm. The structure at the forward edge of the plume base has broken apart by 90 s as the current supplying particles to the plume base begins to wane. An upstream sweeping eddy begins to form at the plume base at 105 s, has grown to a ~20 cm structure with timescale  $> 2$  s by 120 s; by 135 s this structure dominates the plume base. By 150 s the plume has fully detached and the turbulent field records the positions of small, low concentration structures lingering beneath the risen plume.

will rise and their ability to distribute particles (Sparks, 1986; Woods and Kienle, 1994; Calder et al., 1997). Although our experiments were not designed to calculate plume discharges, we can estimate the mass discharge into the plumes as the product of the coignimbrite mass fraction and initial current discharge, yielding discharges of up to 0.9 times the initial current discharge. Such discharges seem high, but are in agreement with mass-balance based calculations of ~57% of the mass erupted as PDCs entering the Mount St. Helens coignimbrite plume (Carey et al., 1990), about half entering plumes at Redoubt Volcano (Woods and Kienle, 1994), and about half entering coignimbrite plumes during the Ksudach KS<sub>1</sub> eruption Gray Phase (Andrews et al., 2007). Calculating the thermal discharge into the plumes is not possible with the measurements we made.

Lastly, that large fractions of the initial currents enter coignimbrite plumes is a reminder that PDC deposits may be unrepresentative of the initial current grain size distributions and componentry. Specifically, as fine-grained and low density particles are more likely to enter the plumes, the deposits should be depleted in those types of particles, particularly for hotter or more energetic (high Ri) currents. Further, dense PDCs can generate ash during transport through particle–particle collisions (Dufek and Manga, 2008), likely resulting in reduced sedimentation rate, increased transfer of thermal energy to entrained air, and thus increased coignimbrite fractionation.

### 5.3. Non-exponential sedimentation from entraining currents

The rate at which deposit thickness decays with distance is strongly affected by Ri and  $TE_b/KE$  of the bulk current. This is not surprising given the effect of those parameters on coignimbrite partitioning and thus reduced sedimentation. As Ri grows, entrainment increases, resulting in increased current thickness, and thus the distance over which particles must fall to sediment from the currents also grows. Increases in current thickness are magnified in currents with high thermal energy densities because the entrained fluid thermally expands and the currents slow and eventually stop forward motion. Consequently, medial and distal regions have enhanced total sedimentation in currents with higher Ri or  $TE_b/KE$  when compared with traditional, exponential models of sedimentation that do not consider entrainment (Fig. 10) (e.g. Dade and Huppert, 1995).

Here we develop a box model for sedimentation in entraining density currents. This model does not account for buoyancy reversal and coignimbrite plume formation, but does explain final deposit profiles. The instantaneous sedimentation rate at any given position is

$$\frac{dM}{dt} = \frac{dcH}{dt} \alpha \frac{Cu_0}{h} \quad 10$$

Eq. (10) can be converted into a spatial derivative using the current velocity

$$\frac{dC}{dx} \alpha \frac{Cu_0}{Uh} \quad 11$$

Because the currents have  $Fr = 1$ , the current velocity is proportional to the square root of particle concentration and current thickness. Observations of the currents show that current thickness grows with the square root of propagation distance, thus Eq. (11) may be rewritten as

$$\frac{dC}{dx} \alpha \frac{C^{2/2}u_0}{h^{3/2}} \alpha \frac{C^{1/2}u_0}{x^{3/4}} \quad 12$$

Integrating Eq. (12) with respect to  $x$  shows that sedimentation,  $S$ , for entraining currents is

$$S(x) \alpha (A_1 - A_2 u_0 x^{1/4})^2 \quad 13$$

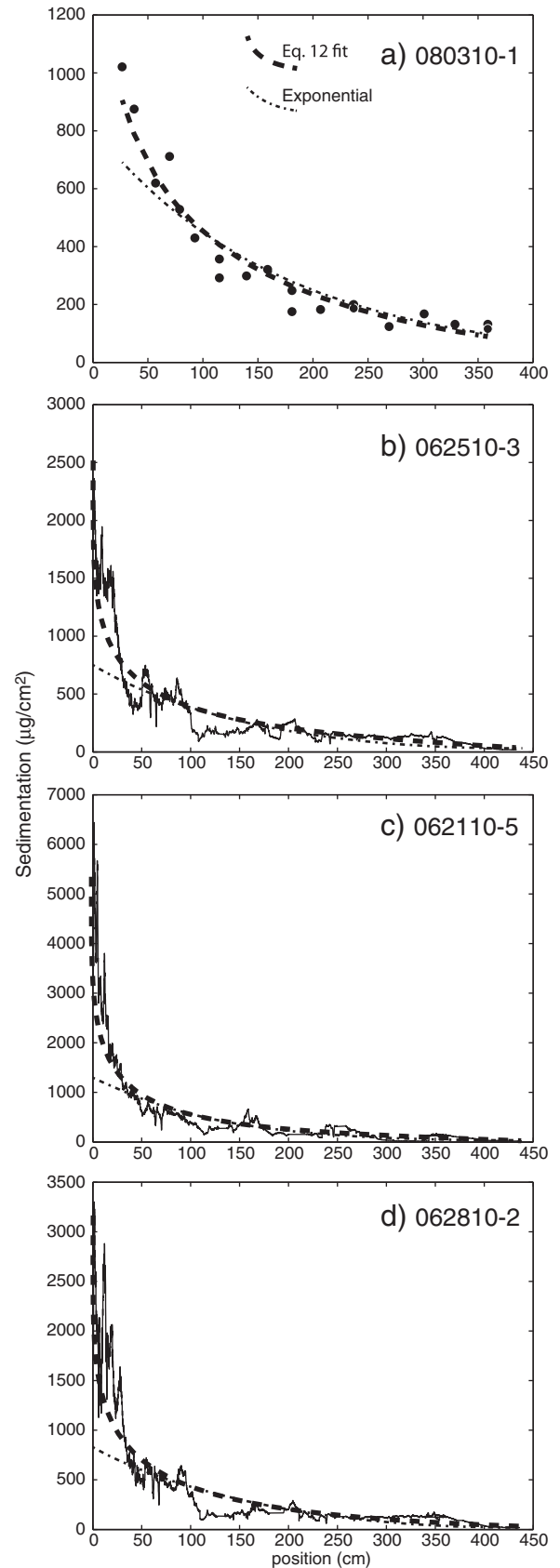


**Fig. 10.** Analytical (Eq. (12)) and exponential fits to sedimentation data for a) a directly measured experiment (080310-1), b) experiment 062510-3, c) experiment 062110-5, and d) experiment 062810-2 that encountered a barrier at 180 cm. The most notable difference in the fits occurs in the proximal regions where Eq. (12) predicts sedimentation closer to the observed values, whereas an exponential fit underpredicts sedimentation.

where  $A_1$  and  $A_2$  are empirical fitting constants related to the initial sediment concentration, current thickness, and fluid entrainment and expansion rates.

Our derived sedimentation expression compares favorably with experimental results over the entire deposit length (Fig. 10). Notably, the expression fits a single curve to the entire deposit rather than fitting multiple exponential curves to different segments of the profile. The expression does not, however, account for secondary thickening beneath coignimbrite plumes.

#### 5.4. Turbulent timescales, sedimentation, and current behavior

Sedimentation is proportional to the time integrated concentration in the lower portions of the currents (Fig. 11), suggesting there is a direct link between particle transport and deposition in our experiments. Further, because the turbulent timescales described in Section 4.4 are a measure of concentration variation through time and space, it is reasonable to think that there are links between turbulence, sedimentation, and general behavior of the currents. Video files in the Supplemental material show a time series of a current, turbulent timescales of concentration variation, and sedimentation rate. The videos document that sedimentation waves are coincident with turbulent structures that propagate near the current base, thus the timescale and sedimentation data are complementary and can provide insights into one another and bulk current behavior.

Evolution of the turbulent structures of the currents during transport is expected given that current density, velocity, and thickness evolve during transport. The bulk of fluid entrainment occurs along the upper surface of the currents, and thus the density of the upper portion of the currents decreases during transport. Moreover, shear between the current and atmosphere act to reduce the velocity of the upper portion of the current. Lastly, the development of this comparatively slow, inflated region effectively isolates the lower portion of the current from interactions with the atmosphere, and thus the currents develop a stratified velocity structure. That a similar structure does not develop at the current head is most likely a result of low density, low velocity regions of the head being stripped rearward into the tail.

During liftoff, the turbulent structures become chaotic. This is most likely the product of three sources of turbulence interacting with one another. First, particle supply into the base of the plume is unsteady as the lower portion of the current alternately flows into the base or up into the plume. Second, eddies at the forward margin of the plume periodically flow into the base of the plume. Third, the

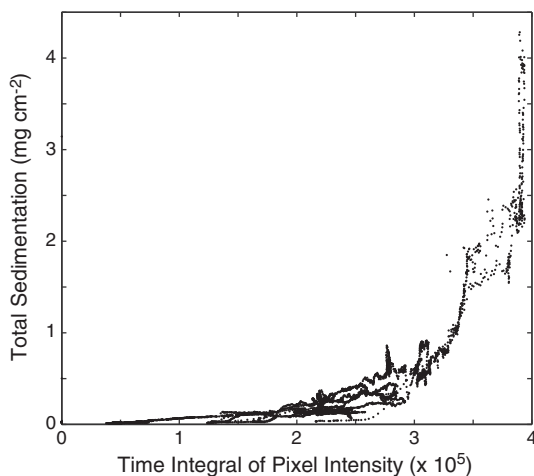


**Fig. 11.** Total sedimentation as a function of the time integral of pixel intensity as measured along the floor of the tank. The regions with integral intensities  $> 3.5 \times 10^5$  are located near the source; their offset results from integration over an interval that includes time after the current has passed.

convective rise of the plume produces unsteady upwelling and downwelling structures at the plume base.

The upstream motion of eddies that occurs during plume detachment is predictable by considering continuity. As the plumes detach from the surface, they draw particles and fluid upward. At the base of the tank, however, the vertical velocity is zero. Continuity thus requires that the upward motion of the detaching plume induces a horizontal flow near the tank floor. That eddies propagate upstream is most likely the result of detachment beginning at the distal reach of the currents and then rolling upstream.

The  $S_T$  and the  $\Sigma_T$  indicate that the particles are in general well-coupled to the turbulent motions of the currents (Burgisser et al., 2005). As a result, sedimentation rates track the eddies because the particles follow the eddies, and regions of high concentration deposit at faster rates. That sedimentation tracks eddies near the base of the currents thus suggests that sedimentation only occurs from the base of the eddies. That is, particles are only deposited from the portions of the eddies nearest the floor. If we consider that near the floor of the tank the vertical component of fluid velocity approaches zero, then we may assume that the local  $\Sigma_T$  is  $> 1$  and thus particles can decouple from the current. The turbulent timescales provide an estimate of the residence time of a particle in this region near the floor, and thus the product of that time with the particle fall velocity is an estimate of the thickness of the current from which sediment may accumulate. In our experiments, with  $\tau = 3$  s and  $u_T = 0.4$  mm/s, this region is  $\sim 1.2$  mm thick. The sedimentation waves thus track the base of the lowest turbulent structures. The initial sedimentation waves that propagate behind the current head record passage of the head and the well defined eddies in the lower portion of the current. Sedimentation patterns become disorganized during liftoff when eddy motions at the plume base are chaotic. Lastly, sedimentation waves record the upstream propagation of eddies during plume detachment.

#### 5.5. Implications for bedforms in PDC deposits

The sedimentation patterns observed in our experiments offer insights into the formation and interpretation of sedimentary structures in natural PDC deposits. In general, massive deposits should form from periods of sustained sedimentation whereas stratified and cross-bedded deposits should record sedimentation at a non-constant rate (Branney and Kokelaar, 2002). Although individual lamina may form through tractional depositional processes (e.g., Dellino and La Volpe, 2000) or cycles of particle accumulation and avalanching (Branney and Kokelaar, 2002), it is unlikely that those processes occur in our very small and comparatively low energy currents. Further, we note that although the particles in our experiments are the size of fine ash, a size that does not typically form tractional bedforms in PDC deposits, the talc particles have similar  $S_T$  and  $\Sigma_T$  as 100 to 300  $\mu\text{m}$  ash transported by pyroclastic surges; ash of that size range is commonly deposited in laminated and cross-laminated bedforms by PDCs. Our experiments are thus applicable to natural PDCs if we consider how dilute currents supply their underlying depositional systems. Depositional systems with particle residence times equal to or less than the eddy timescales should preserve depositional signals related to turbulence within the current, whereas records of turbulence should be attenuated in systems with longer residence times.

That sedimentation waves track individual turbulent structures suggests that each lamina records the passage of a large eddy. Individual laminations record deposition over a time interval approximately equal to the characteristic timescale of the eddy. Although occasional turbulent structures persist through the length of the current, individual eddies generally evolve through time and space and only remain recognizable for a few turbulent timescales (Bernard and Wallace, 2002). Consequently, we should expect that individual lamina should be deposited over distances no greater than 2–3 times the

characteristic eddy lengthscale,  $\Lambda$ , and more commonly over distances approximately equal to  $\Lambda$ .

The sedimentation patterns recorded in our experiments thus provide insight into the extent of individual laminations and how packages of laminations may be used to estimate transport characteristics of PDCs. If we assume a dilute current with average velocity of 30 m/s, total thickness of 200 m, and  $\Lambda = 0.5 h$ , then the current has a turbulent, and thus depositional, timescale of  $\sim 3$  s. The greatest extent of any single lamination within its deposits should be  $< 300$  m, and most layers should be present over approximately 100 m. If the particles suspended in this current have 0.25 mm diameters and densities of 2000 kg/m<sup>3</sup>, then they should have fall velocities of  $\sim 3.4$  m/s, and thus the lower  $\sim 10$  m of the eddies should be sampled by the deposits. Each lamination records approximately 3 s of the current, but there are likely similar intervals of reduced deposition or erosion between each well-sorted lamination. A sequence of  $n$  laminations with timescale  $\tau$ , records a depositional time  $t_{dep}$  on the order of

$$t_{dep} = 2n\tau. \quad 14$$

For example, a 0.5-m thick sequence of 1-cm laminations each recording 3 s of the example current records  $\sim 300$  s of total depositional time.

Many PDC deposits contain cross-stratified laminations. Although the deposits within our currents are too thin to examine directly, the periodic and directional natures of deposition suggest that they should be cross stratified. We expect that the depositional–erosional couplets that compose each sedimentation wave should produce sequences of cross-stratified laminations dipping in the direction of transport. Cross-stratification should be particularly common beneath the rising plumes where sedimentation waves become disorganized; within these regions the orientation of cross-laminated units should be irregular, reflecting the unsteady and variable propagation of eddies.

Anti-dunes are also found in many PDC deposits. These units, cross-stratified with laminations dipping in the “upstream” direction (toward the volcano), are generally interpreted in the context of research conducted in fluvial and subaqueous systems relating bedforms to various flow regimes (Cole, 1991; Bryan, et al., 1998; Valentine and Fisher, 2000; Branney and Kokelaar, 2002; Brown and Branney, 2004). In fluvial systems, anti-dunes are deposited beneath an upstream propagating surface wave and indicate supercritical flow conditions ( $Fr > 1$ ). In subaerial systems, however, there is very little density contrast between dilute currents and the atmosphere, and thus there is at best a subtle free surface to form an upstream propagating wave. In the lower parts of PDCs, greater density contrasts may exist between regions dominated by particle–particle interactions or tractional processes and more dilute regions, but the interface between the dilute and dense regions may be gradational and unsteady (e.g. Branney and Kokelaar, 1992; Branney and Kokelaar, 1997). Consequently, interpretations of supercritical flow in PDCs may be inappropriate in some instances. Indeed, where anti-dunes have been observed forming in aeolian systems, formation occurs through adhesion of particles on the wet stoss faces of dunes; these “anti-dunes” are actually adhesion ripples and form through an entirely different process than subaqueous bedforms (Kocurek and Fielder, 1982). In our experiments, sedimentation waves often propagate up to  $\sim 0.3$  of the total runout distance following plume detachment, and these waves should form cross-stratified deposits as they are otherwise indistinguishable from downstream-propagating sedimentation waves. These cross-stratified units, however, should dip toward the particle source, thus the units would appear to be anti-dunes but are in fact dunes that record flow reversal. Importantly, even if a tractional depositional system supplied by the dilute current is required for the formation of cross-stratified deposits, that system should change direction to record a flow reversal provided the

duration of the reversal is longer than the particle residence time within the depositional system. Our experiments suggest that some “anti-dunes” in PDC deposits, particularly in regions where coignimbrite plumes were likely generated, are not “anti” but instead record reversals in the flow direction.

## 6. Summary

Sedimentation from dilute PDCs does not necessarily follow an exponential decay with distance, and deposits frequently become chaotic in distal regions, reflecting the importance of air entrainment and thermal expansion during transport and buoyant liftoff. Very large fractions of fine-grained material initially transported by PDCs do not accumulate in PDC deposits but are instead elutriated into coignimbrite plumes. Coignimbrite mass depends upon excess thermal energy, and coignimbrite fractionation depends on  $Ri$  and  $TE_b/KE$  of the current. Sedimentation rate is not constant but rather propagates as a series of depositional and erosional waves through the system; these waves record transit of the largest turbulent structures in the currents. Flow reversals often occur when coignimbrite plumes form, resulting in backward propagation of eddies and sedimentation waves, suggesting that anti-dune structures may record local flow reversals, not necessarily supercritical flows.

Supplementary materials related to this article can be found online at doi:10.1016/j.jvolgeores.2012.02.011.

## Acknowledgments

BJA was supported by the NSF Earth Sciences Postdoctoral Fellowship program under grant EAR-0847366. MM was supported by NSF grant EAR-080954. The experimental facility was constructed at UC Richmond Field Station with the assistance of Stuart Foster in a space provided by Leonard Sklar and Bill Dietrich. William Gange assisted with running many experiments. James E. Gardner graciously provided grain size analyses of the talc powder. Thoughtful reviews by G. Lube and P. Dellino improved this paper.

## References

- Andrews, B.J., Manga, M., 2011. Effects of topography on pyroclastic density current runout and formation of coignimbrites. *Geology* 39, 1099–1102.
- Andrews, B.J., Gardner, J.E., Tait, S., Ponomareva, V., Melekestsev, I.V., 2007. Dynamics of the 1800 <sup>14</sup>C yr BP caldera-forming eruption of Ksudach Volcano, Kamchatka, Russia. In: Eichelberger, J., Gordeev, E., Kasahara, M., Izbekov, P., Lees, J. (Eds.), *Volcanism and Subduction: The Kamchatka Region: Geophysical Monograph*, 172, pp. 325–342.
- Andrews, B.J., Cardenas, M.B., Bennett, P.C., 2011. Analysis of turbulent non-isothermal mixing between a jet and cooler ambient water using thermal imagery. *Geochemistry, Geophysics, Geosystems* 12, Q07022. doi:10.1029/2011GC003530.
- Bernard, P.S., Wallace, J.M., 2002. *Turbulent Flow: Analysis, Measurement, and Prediction*. Hoboken, New Jersey, Wiley. 512 pp.
- Branney, M.J., Kokelaar, P., 1992. A reappraisal of ignimbrite emplacement; progressive aggradation and changes from particulate to non-particulate flow during emplacement of high-grade ignimbrite. *Bulletin of Volcanology* 54, 504–520.
- Branney, M.J., Kokelaar, P., 1997. Giant bed from a sustained catastrophic density current flowing over flat topography: Acatlán ignimbrite, Mexico. *Geology* 25, 115–118.
- Branney, M.J., Kokelaar, B.P., 2002. Pyroclastic density currents and the sedimentation of ignimbrites. *Memoirs of the Geological Society of London*, 27, 143 pp.
- Brown, R.J., Branney, M.J., 2004. Bypassing and diachronous deposition from density currents: evidence from a giant regressive bed form in the Poris ignimbrite, Tenerife, Canary Islands. *Geology* 32, 445–448.
- Browne, B.L., Gardner, J.E., 2005. Transport and deposition of pyroclastic. *Bulletin of Volcanology* 67, 469–489.
- Bryan, S.E., Cas, R.A.F., Marti, J., 1998. Lithic breccias in intermediate volume phonolitic ignimbrites, Tenerife (Canary Islands): constraints on pyroclastic flow depositional processes. *Journal of Volcanology and Geothermal Research* 81, 269–296.
- Burgisser, A., Bergantz, G.W., Breidenthal, R.E., 2005. Addressing the complexity in laboratory experiments: the scaling of dilute multiphase flows in magmatic systems. *Journal of Volcanology and Geothermal Research* 141, 245–265. doi:10.1016/j.jvolgeores.2004.11.001.
- Bursik, M.I., Woods, A.W., 1996. The dynamics and thermodynamics of large ash flows. *Bulletin of Volcanology* 58, 175–193.

- Bursik, M.I., Woods, A.W., 2000. The effects of topography on sedimentation from particle-laden turbulent density currents. *Journal of Sedimentary Research* 70, 53–63.
- Bursik, M.I., Kurbatov, A.V., Sheridan, M.F., Woods, A.W., 1998. Transport and deposition in the May 18, 1980, Mount St. Helens blast flow. *Geology* 26, 155–158.
- Calder, E.S., Sparks, R.S.J., Woods, A.W., 1997. Dynamics of co-ignimbrite plumes generated from pyroclastic flows of Mount St. Helens (7 August 1980). *Bulletin of Volcanology* 58, 432–440.
- Calder, E.S., Sparks, R.S.J., Gardeweg, M.C., 2000. Erosion, transport and segregation of pumice and lithic clasts inferred from ignimbrite at Lascar Volcano, Chile. *Journal of Volcanology and Geothermal Research* 104, 201–235.
- Carey, S., Sigurdsson, H., Gardner, J.E., Criswell, W., 1990. Variations in column height and magma discharge during the May 18, 1980 eruption of Mount St. Helens. *Journal of Volcanology and Geothermal Research* 43, 99–112.
- Cole, P.D., 1991. Migration direction of sand-wave structures in pyroclastic-surge deposits: implications for depositional processes. *Geology* 19, 1108–1111.
- Dade, B.W., Huppert, H.E., 1995. A Box Model for Non-entraining Suspension-driven Gravity Surges on Horizontal Surfaces.
- Dade, W.B., Huppert, H.E., 1996. Emplacement of the Taupo ignimbrite by a dilute turbulent flow. *Nature* 381, 509–512.
- Dellino, P., La Volpe, L., 2000. Structures and grain size distributions in surge deposits as a tool for modeling the dynamics of dilute pyroclastic density currents at La Fossa di Vulcano (Aeolian Islands, Italy). *Journal of Volcanology and Geothermal Research* 96, 57–78.
- Dellino, P., Buttner, R., Dioguardi, F., Doronzo, D.M., La Volpe, L., Mele, D., Sonder, I., Sulpizio, R., Zimanowski, B., 2010. Experimental evidence links volcanic particle characteristics to pyroclastic flow hazard. *Earth and Planetary Science Letters* 295, 314–320.
- Doronzo, M.D., Valentine, G.A., Dellino, P., de Tullio, M.D., 2010. Numerical analysis of the effect of topography on deposition from dilute pyroclastic density currents. *Earth and Planetary Science Letters*. doi:10.1016/j.epsl.2010.10.003.
- Druitt, T.H., Calder, E.S., Cole, D., Hoblitt, R.P., Loughlin, S.C., Norton, G.E., Ritchie, L.J., Sparks, R.S.J., Voight, B., 2002. Small-volume, highly mobile pyroclastic flows formed by rapid sedimentation from pyroclastic surges at Soufriere Hills Volcano, Montserrat: an important volcanic hazard. In: Druitt, T.H., Kokelaar, B.P. (Eds.), *The Eruption of Soufriere Hills Volcano, Montserrat, from 1995 to 1999*: Geol. Soc. Lond. Mem., 21, pp. 263–279.
- Dufek, J., Bergantz, G.W., 2007. Suspended load and bed-load transport of particle-laden gravity currents: the role of particle-bed interaction. *Theoretical and Computational Fluid Dynamics* 21, 119–145. doi:10.1007/s00162-007-0041-6.
- Dufek, J., Manga, M., 2008. In situ production of ash in pyroclastic flows. *Journal of Geophysical Research* 113, B09207.
- Fierstein, J.E., Nathenson, M., 1992. Another look at the calculation of fallout tephra volumes. *Bulletin of Volcanology* 54, 156–167.
- Fisher, R.V., Orsi, G., Ort, M.H., Heiken, G., 1993. Mobility of a large-volume pyroclastic flow — emplacement of the Campanian ignimbrite, Italy. *Journal of Volcanology and Geothermal Research* 56, 205–220.
- Freundt, A., 2003. Entrance of hot pyroclastic flows into the sea: experimental observations. *Bulletin of Volcanology* 65, 144–164.
- Fujii, T., Nakada, S., 1999. The 15 September 1991 pyroclastic flows at Unzen Volcano (Japan): a flow model for associated ash-cloud surges. *Journal of Volcanology and Geothermal Research* 89, 159–172.
- Gardner, J.E., Burgisser, A., Stelling, P., 2007. Eruption and deposition of the Fisher Tuff (Alaska): evidence for the evolution of pyroclastic flows. *Journal of Geology* 115, 417–435.
- Girolami, L., Roche, O., Druitt, T.H., Corpetti, T., 2010. Particle velocity fields and depositional processes in laboratory ash flows, with implications for the sedimentation of dense pyroclastic flows. *Bulletin of Volcanology* 71, 747–759.
- Houghton, B.F., Wilson, C.J.N., Fierstein, J., Hildreth, W., 2004. Complex proximal deposition during the eruptions of 1912 at Novarupta, Alaska. *Bulletin of Volcanology* 66 (95), 133.
- Kocurek, G., Fielder, G., 1982. Adhesion structures. *Journal of Sedimentary Petrology* 52, 1229–1241.
- Lube, G., Huppert, H.E., Sparks, R.S.J., Hallworth, M.A., 2004. Axisymmetric collapses of granular columns. *Journal of Fluid Mechanics* 508, 175–199. doi:10.1017/S0022112004009036.
- Macias, J.L., Capra, L., Arce, J.L., Espindola, J.M., Carcia-Palomo, Sheridan, M.F., 2008. Hazard map of El Chichón volcano, Chiapas, Mexico: constraints posed by eruptive history and computer simulations. *Journal of Volcanology and Geothermal Research* 175, 444–458.
- Sigurdsson, H., Carey, S., 1989. Plinian and co-ignimbrite tephra fall from the 1815 eruption of Tambora volcano. *Bulletin of Volcanology* 51, 243–270.
- Simpson, J.E., 1997. *Gravity Currents in the Environment and Laboratory*. Cambridge University Press, Cambridge.
- Sparks, R.S.J., 1986. The dimensions and dynamics of volcanic eruption columns. *Bulletin of Volcanology* 48, 3–15.
- Sparks, R.S.J., Gardeweg, M.C., Calder, E.S., Matthews, S.J., 1997. Erosion by pyroclastic flows on Lascar Volcano, Chile. *Bulletin of Volcanology* 58, 557–565.
- Stroberg, T.W., Manga, M., Dufek, J., 2010. Heat transfer coefficients of natural volcanic clasts. *Journal of Volcanology and Geothermal Research* 96, 214–291.
- Valentine, G.A., Fisher, R.V., 2000. Pyroclastic surges and blasts. In: Sigurdsson, H., Houghton, B., McNutt, S.R., Rymer, H., Stix, J. (Eds.), *Encyclopedia of Volcanoes*, pp. 571–580.
- Vasquez, J.A., Ort, M.H., 2006. Facies variation of eruption units produced by the passage of single pyroclastic surge currents, Hopi Buttes volcanic fields, USA. *Journal of Volcanology and Geothermal Research* 154, 222–236.
- Wilson, C.J.N., 2008. Supereruptions and supervolcanoes: processes and products. *Elements* 4, 29–34. doi:10.2113/GSELEMENTS.4.1.29.
- Wilson, C.J.N., Walker, G.P.L., 1982. Ignimbrite depositional facies: the anatomy of a pyroclastic flow. *Journal of the Geological Society of London* 139, 581–592.
- Woods, A.W., Kienle, J., 1994. The dynamics and thermodynamics of volcanic clouds: theory and observations from the April 15 and April 21, 1990 eruptions of Redoubt Volcano, Alaska. *Journal of Volcanology and Geothermal Research* 62, 273–299.